RSC Advances

This is an *Accepted Manuscript*, which has been through the Royal Society of Chemistry peer review process and has been accepted for publication.

Accepted Manuscripts are published online shortly after acceptance, before technical editing, formatting and proof reading. Using this free service, authors can make their results available to the community, in citable form, before we publish the edited article. This *Accepted Manuscript* will be replaced by the edited, formatted and paginated article as soon as this is available.

You can find more information about *Accepted Manuscripts* in the Information for Authors.

Please note that technical editing may introduce minor changes to the text and/or graphics, which may alter content. The journal's standard Terms & Conditions and the Ethical guidelines still apply. In no event shall the Royal Society of Chemistry be held responsible for any errors or omissions in this *Accepted Manuscript* or any consequences arising from the use of any information it contains.

ROYAL SOCIETY OF CHEMISTRY

www.rsc.org/advances

Enhanced photocatalytic activity of g-C_3N_4-ZnO/HNTs composite heterostructure photocatalysts for degradation of tetracycline under visible light irradiation

[a]Jinze Li, [a]Mingjun Zhou, [a]Zhefei Ye, [b]Huiqin Wang, [b]Changchang Ma, [a]Pengwei Huo*, [a]Yongsheng Yan*

[a]*School of Chemistry & Chemical Engineering, Jiangsu University, Zhenjiang 212013, People's Republic of China,*

[b]*School of Environment, Jiangsu University, Zhenjiang 212013, People's Republic of China,*

RSC Advances Accepted Manuscript

* Corresponding author Tel.: +86 511 8879 0187 Fax. : +86 511 8879 1800
E-mail address: huopw@mail.ujs.edu.cn(P.W. Huo); yys@mail.ujs.edu.cn(Y.S. Yan)

Abstract

A novel graphitic carbon nitride (g-C_3N_4)-ZnO/halloysite nanotubes (HNTs) nanocomposite photocatalyst was synthesized via a facile calcination method in order to enhance the visible-light photocatalytic activity and stability of pure ZnO photocatalysts for degradation of tetracycline. The network-layered structure of g-C_3N_4 was formed after compositing with previously prepared ZnO/HNTs and the g-C_3N_4-ZnO heterojunction has been formed during the coupling process. Furthermore, the HNTs can efficiently extend the surface area of g-C_3N_4, which lead to strengthening the pathways of charge transfer and prolonging the lifetimes of photoexcited carriers. Electrochemical impedance spectroscopy (EIS) and Incident-photon-to-current conversion efficiencies (IPCE) measurements showed the improvement of as-obtained g-C_3N_4-ZnO/HNTs photocatalysts performance which can be attributed to the enhanced charge transfer as a result of more effective separation of photogererated electron-hole pairs. Such a notable enhancement of photocatalytic performances were mainly ascribed to the improved charge transfer and separation rate of photogenerated electron-hole pairs by the heterostructure of g-C_3N_4-ZnO/HNTs catalyst. The mechanism of photodegradation was systematically analysed by active species trapping text and electron spin resonance (ESR) spin-trap technique with dimethyl pyridine N-oxide (DMPO), which conclude that the •OH and •O_2^- radicals are the major reactive species during the photocatalytic reaction for g-C_3N_4-ZnO/HNTs composite photocatalysts.

Keywords: Visible light; Heterojunction; g-C_3N_4-ZnO/HNTs; Photo stability;

RSC Advances Accepted Manuscript

1. Introduction

Photocatalysis, as an environmental friendly technology, offers great potential for complete removal of organic chemical pollutants. It has been reported that the nano-structural semiconductor metal oxides photocatalyst can degrade various organic pollutants under UV-visible light irradiation [1]. In recent years, a large number of semiconductor metal oxides and sulphides photocatalysts, such as TiO_2 [2-4], ZnO [5], CdS [6], Fe_2O_3 [7], Bi_2WO_6 [8] and so on, have been made to develop efficient photocatalysts. As a promising semiconductor material, ZnO has received great attention owing to its high activity, low cost and environmentally friendly feature. Furthermore, nano-sized ZnO has a high UV-vis response ability because of its wide band gap (~3.37eV) and large exaction binding energy (60 meV)[9], which possesses higher photocatalytic efficiency than TiO_2. Unfortunately, there are still several issues limiting the application of pure ZnO nanoparticle for photocatalysis, one of them is the high recombination rate of photogenerated electron-hole pairs. Simultaneously, photocorrosion of ZnO is particularly prone to occur in photocatalytic reaction which caused by the oxidation of ZnO by photogenerated holes[5, 10]. The narrow light-responsive range is also a fundamental issue hindering the large-scale application of ZnO in industry[11]. Therefore, numerous efforts have been made to improve the photocatalytic performance of ZnO nanomaterials via different strategies, such as coupling with other components [12-14], doping [9, 15], surface modification with metal nanoparticles [5, 16, 17], and developing heterostructure [18]. Among these, combining ZnO with other semiconductors to form heterojunction with a suitable band structure

RSC Advances Accepted Manuscript

can efficaciously extend light-absorption range and accelerate the separation rate of electron-hole pairs.

Recently, a metal-free photocatalyst, polymeric g-C_3N_4 has attracted much attention, because of its high thermal and chemical stability, suitable band gap, and easy preparation[19-23]. These special properties make g-C_3N_4 a better material for organic pollutant degradation, splitting water for producing H_2, and CO_2 reduction[24]. Being regarded as a visible light sensitizers, g-C_3N_4 possesses several advantages towards other photocatalysts. Several kinds of g-C_3N_4 composite photocatalysts have been fabricated by coupling g-C_3N_4 with other types of inorganic photocatalysts, such as TiO_2/g-C_3N_4 [25, 26], Ag-AgBr/g-C_3N_4 [26, 27], CdS/g-C_3N_4[28], g-C_3N_4/Bi_2WO_6[29], g-C_3N_4-Ag_3PO_4 [30], etc. Most of these composite semiconductors are responsive to visible light, because of the doped semiconductors with narrow band gaps which can strengthen the photocatalytic activity in solar light. Coating ZnO with g-C_3N_4 has been shown to be advantageous, not only owing to the enhanced visible light response, but also for the charge separation in the photoexcited electron-hole pairs. Therefore, it needs a suitable material as the carrier for prepared higher performance photocatalysts. However, the nano-particles are always easy to aggregate, which could greatly reduce the surface area and the reacted sites to degrade the photocatalytic performance. Therefore, many researchers devote to loaded supporters and enhance the performance of nano-particles, such as carbon materials, mineral substance, and so forth. As a promising mineral supporter materials, HNTs are a two-layered nature clay mineral, with aluminol (Al-OH) groups in internal

RSC Advances Accepted Manuscript

surface and Si-O-Si on the external surface[31]. HNTs in a position to disperse nanoparticles onto their surface to improve the stability of nanoparticles because of their large surface and inherent nanotube structure. There are several studies about the synthesis of HNTs coupled with other nanomaterials, which have been proved to possess promising performance as a catalyst carrier. Xing et al. reported the CdS/HNTs nanocomposites which synthesized by hydrothermal method[32]. Cavallaro's group reported HNTs modified by sodium alkanoates which evidenced to obtain rather stable aqueous nanoclay dispersions[33]. And Makaremi et al. investigated the electrospun nanofibrous membranes of polyacrylonitrile/HNTs with superior water filtration ability[34]. Above all these studies displayed the excellent dispersity and stability of HNTs.

Herein, in our work, to sufficiently utilize the advantages of relatively high stability, suitable optical band gap (2.7 eV) and well photocatalytic activity of g-C_3N_4, large surface of HNTs, respectively, the g-C_3N_4-ZnO/HNTs nanocomposite photocatalyst was successfully synthesized by us via a facile two-step calcination method which can effectively prolong the lifetimes of photoexcited charge carriers. Furthermore, the specific layered-netlike structure of g-C_3N_4 was greatly utilized to wrap the ZnO/HNTs which contributed to suppress the photocorrosion of ZnO nanoparticles and enhanced the photo-stability of the g-C_3N_4-ZnO/HNTs composite photocatalyst. The abuse of antibiotics, such as tetracycline (TC), ciprofloxacin, norfloxacin and so on, is now a major crisis for public health agencies and leaders across the globe[35, 36], which have aroused particular attention because of their

RSC Advances Accepted Manuscript

excessive application to medical, agriculture, and biology. The visible light photocatalytic tests show that the present g-C_3N_4-ZnO/HNTs composites possess much higher photocatalytic activity and photostability after four successive cycles than those of either individual ZnO or C_3N_4, and ZnO/HNTs for TC degradation under visible light irradiation. The photoelectrical properties were detected by IPCE and EIS. In addition, the ESR was introduced to investigate the possible photocatalytic mechanism during the photocatalytic degradation system.

2. Experiment

2.1 Materials

Zinc nitrate hexahydrate ($Zn(NO_3)_2 \cdot 6H_2O$, Pur. ≥99.0%), $C_3H_6N_6$, and ethanol (Pur. >99.5%) were supplied by Sinopharm Chemical Reagent Co., Ltd. China. HNTs were purchased from Zhengzhou Jin yang guang Chinaware Co., Ltd. Henan, China. (>99%). Tetracycline (TC) was purchased from Shanghai Shunbo Biological Engineering Co., Ltd. All reagents for synthesis and analysis were used without further purification. Deionized water was used throughout this work.

2.2. Preparation of photocatalysts

First, 1.0 g of HNTs were put into 250 mL different concentrations of $Zn(NO_3)_2$ solution under continuous magnetic stirring for 2 h. Then, heating and evaporating suspension to dryness, the resultant product was milled into a powder and collected in an alumina crucible, the drying sample was calcined at different temperatures for 3 h in muffle furnace to synthesize the ZnO/HNTs photocatalysts. The pure g-C_3N_4 powders were prepared by directly calcining melamine at 520 °C for 3 h. Next, the

RSC Advances Accepted Manuscript

typical preparation of g-C_3N_4-ZnO/HNTs catalysts was as follows: melamine powder and ZnO/HNTs samples with mass ratio of 5wt.%,10wt.%, 20wt.%, 50wt.% and 100wt.% were heated to 450 °C at a heating rate of 10 °C min^{-1} in a muffle furnace and maintained for 2 h[37,38]. After the alumina crucible was cooled down to room temperature, the as-prepared sample were collected and ground into powder. The final composite g-C_3N_4-ZnO/HNTs photocatalysts were obtained. The synthesis process is illustrated in **Fig. 1**.

Fig. 1. The schematic illustration on formation of g-C_3N_4-ZnO/HNTs composite photocatalysts.

2.3. Characterization of Matrials

The crystal structure was analyzed by X-ray diffraction (XRD model MAC Science, Japan) with Ni-filtrated Cu Kα radiation. The scan range of 2θ was 5-80° at a scan rate of 5°/min. The transmission electron microscopy (TEM) and high-resolution transmission electron microscopy (HRTEM) images were examined by transmission electron microscopy (JEM-2010, Japan). The scanning electron microscopy (SEM) pictures were characterized by a field emission scanning electron microscopy (FE-SEM, JSM-7001F, Japan). Energy dispersive X-ray spectroscopy (EDS) was taken on a FEI Tecnai G2F20 instrument and operated at an accelerating voltage of 200 kV. The X-ray photoelectron spectroscopy (XPS) measurements were carried on a PerkinElmer PHI 5300 instrument using Al Kα radiation and the C1s signal was set to the position of 284.6 eV. The diffuse reflectance spectra (DRS) of the catalysts were performed in the range of 250-850 nm using a UV-vis

RSC Advances Accepted Manuscript

spectrophotometer (UV-2450; Shimazu, Japan) equipped with an integrating sphere. Specific surface area was detected by the Brunauer-Emmett-Teller (BET) technique from the N_2 adsorption isotherm, the pore size distribution was determined by desorption isotherm using the Barrett-Joiner-Halenda (BJH) method. The photoluminescence (PL) spectra for solid samples were performed by an F-4500 (Hitachi, Japan) photoluminescence detector.

2.4. Photocatalytic Activity Test

The photocatalytic activities of the synthesized photocatalysts were evaluated by the degradation of 20 mg/L TC under visible-light irradiation. A 350 W Xenon arc lamp was used as the light source of the photocatalytic reaction. The reaction system contains TC solution (100 mL, 20 mg/L) and g-C_3N_4-ZnO/HNTs photocatalysts (0.1g) with recycling water (30°C) to maintain a constant reactor temperature. Prior to irradiation, the mixture was stirred under dark conditions for 30 min to ensure that the adsorption-desorption equilibrium was reached. Sampling periodically from the suspension and centrifuged at a given 10 min interval to measure the absorbancye of TC with a UV-vis spectrophotometer at a wavelength of 357 nm.

3. Results and discussion

3.1. XRD analysis

The XRD patterns of the pure ZnO, g-C_3N_4 and composited photocatalysts are shown in **Fig. 2**a. It is observed two distinct peaks at 27.4° and 13.1° of the pure g-C_3N_4 could be assigned to the (002) and (100) diffraction planes (JCPDS 87-1526)

RSC Advances Accepted Manuscript

in g-C_3N_4-ZnO/HNTs composite photocatalysts, which correspond to the characteristic interplanar staking peaks of aromatic systems and the interlayer structural packing, respectively. And compared with the as-prepared composite photocatalysts, the diffraction peaks of ZnO are also obviously shown in **Fig. 2**a, g-C_3N_4-ZnO/HNTs, which could be indexed as the hexagonal wurtzite crystal phase of ZnO (JCPDS 65-3411). **Fig. 2**b displays the different mass ratio of g-C_3N_4. It is noteworthy that there is a sharp peak located at 26.9° which could be identified as the (003) diffraction for Halloysite[34]. With increasing g-C_3N_4 proportion, the diffraction peaks of g-C_3N_4 became stronger, while those of Halloysite are weaker. It is possibly attributed that the peaks of Halloysite could be covered by g-C_3N_4[31]. Besides, no obvious phase of Halloysite is observed in the composite photocatalysts because of the overlapped with ZnO. Expect for ZnO, g-C_3N_4 and HNTs, no other phases are detected.

Fig. 2. XRD patterns of (a) pure ZnO, g-C_3N_4 and g-C_3N_4-ZnO/HNTs and (b) different content of g-C_3N_4 composite photocatalysts.

3.2. SEM, EDS, TEM and HRTEM

The morphology and microstructure of HNTs, ZnO/HNTs, and g-C_3N_4-ZnO/HNTs were investigated by SEM, TEM, HRTEM, and EDS, respectively. **Fig. 3**a shows the SEM images of pure HNTs, it is clearly that HNTs displays a cylindrical-shaped tubular structure which aligned randomly, with a diameter in the range of 80-150 nm,

RSC Advances Accepted Manuscript

and the length of nanotubes are around 0.2-1.2 μm. It can be clearly observed that the surface of nanotubes is level and smooth. As shown in **Fig. 3**c and **Fig. 4**b, amounts of varied sphere-like ZnO nanoparticles with the diameter of 10-80 nm, which are deposited on the surface of HNTs. **Fig. 3**c shows the SEM of the g-C_3N_4-ZnO/HNTs which displayed an aggregated layered structure with a smooth surface[38]. As shown in the TEM image (**Fig. 4**c), after introducing g-C_3N_4, the HNTs with the ZnO nanoparticles are found to embed and distribute among the g-C_3N_4 network structure, which results in forming a g-C_3N_4-ZnO heterojunction.

In order to get further information about the heterojunction of ZnO-g-C_3N_4, high-resolution transmission electron microscopy (HRTEM) analysis was performed. It can be seen that two different phases combine each other closely in **Fig. 4**d of g-C_3N_4-ZnO. The dark phase, which exhibits a clear lattice fringe should be ascribed to ZnO, and the *d* spacing value is 0.281 nm, corresponding to the (100) crystallographic plane of hexagonal wurtzite crystal ZnO nanoparticle[13]. The other phase without fringes can be assigned to g-C_3N_4. The observed interface between semiconductors would favor the spatial separation and extend lifetimes of photogenerated electron-hole pairs, which reduces the internal charge recombination and increase photocatalytic activity. Furthermore, it is very interesting that the hetero-architectures between ZnO nanoparticles and HNTs, g-C_3N_4 and HNTs (there are not shown) may be also well-formed [3, 39]. These deduces will be confirmed in the following work.

Fig. 3b, d, and f are EDS spectra of the samples HNTs, ZnO/HNTs, and

RSC Advances Accepted Manuscript

g-C_3N_4-ZnO/HNTs, respectively. It is indicated that Al, Si, and O elements existed in pure HNTs (**Fig. 3**b). As shown in **Fig. 3**d, Zn, O elements are also existed in ZnO/HNTs composite photocatalyst. According to **Fig. 3**f, the as-prepared photocatalysts consist of Al, Si, O, Zn, C and N. The EDS spectrum further confirmed that the g-C_3N_4-ZnO/HNTs composite catalysts are successfully fabricated.

Fig. 3. SEM and EDS images of (a, b) HNTs, (c, d) ZnO/HNTs, (e, f) g-C_3N_4-ZnO/HNTs.

Fig. 4. (a) TEM image of pure HNTs. (b) TEM image of ZnO/HNTs. (c) TEM image of g-C_3N_4-ZnO/HNTs. (d) HRTEM image of g-C_3N_4-ZnO/HNTs photocatalysts.

3.3. FT-IR

The FT-IR spectra of pure HNTs, pure g-C_3N_4 and g-C_3N_4-ZnO/HNTs photocatalysts are shown in **Fig. S1**. The adsorption bands at 3697 and 3622 cm^{-1} are ascribed to the -OH groups. The band at 1035 and 450-550 cm^{-1} can be assigned to the Si-O stretching and Si-O bending vibrations, respectively. The peak at 910 cm^{-1} is due to the O-H deformation vibration of inner Al-OH groups (between the interface of the Al-O octahedron and the Si-O tetrahedron) for HNTs[40]. In the FT-IR spectrum of g-C_3N_4, the relative strong peaks are concentrated in the 1200-1650 cm^{-1} region in the spectrum, the absorption band at 1635 cm^{-1} is attributable to the C=N stretching, while the three at 1240, 1322 and 1402 cm^{-1} are due to the aromatic C-N stretching[25, 41]. The peak at 808 cm^{-1} is attributed to out-of-plane bending modes of C-N heterocycles[42]. This result is consistent with that of the XRD analysis. All of these adsorption bands

RSC Advances Accepted Manuscript

for HNTs and g-C_3N_4 can be observed in the FT-IR spectrum of g-C_3N_4-ZnO/HNTs, and suggesting that no structural change of g-C_3N_4 occurs. In addition, the characteristic peaks of ZnO which should have been clearly observed at about 623 and 460 cm^{-1}, identified to the vibration of Zn-O-Zn and Zn-O, respectively, belonging to ZnO nanoparticles and g-C_3N_4-ZnO heteroarchitectures. This may be due to that these peaks of ZnO are overlapped by the peaks of HNTs. All of these FT-IR spectra provided the valuable information which indicating that the g-C_3N_4-ZnO heterojunction is successfully formed and excellently attached to the HNTs.

3.4. XPS spectra of g-C_3N_4-ZnO/HNTs

To further determine the chemical state of elements and composition of the g-C_3N_4-ZnO/HNTs, the XPS measurements were carried out, as shown in **Fig. 5**. **Fig. 5**a displays the XPS spectra of g-C_3N_4-ZnO/HNTs, the peaks related to Zn, O, C, N and a small amount of elements of HNTs, such as Al and Si. As shown in **Fig. 5**b, two main carbon peaks represented in the C1s spectra for g-C_3N_4 at the binding energies of 284.6 eV and 288.1 eV, respectively. The peak located at 284.6 eV is corresponding to sp^2 C-C bonds, and the other peak at 288.1 eV is assigned to sp^2-hybridized carbon in N-containing aromatic ring (N-C=N) [43]. Both of them exhibit the existence of g-C_3N_4. The N1s features are observed in **Fig. 5**c can be fitted into two peaks, which should be ascribed to C-N=C (397.9 eV), tertiary nitrogen N-$(C)_3$ (400.1 eV), respectively. **Fig. 5**d shows the O1s peaks at 532.6 eV and 530.1 eV. The high energy peak (at 532.6 eV) is attributed to oxygen which making single bond carbon (C-O), and the low energy

RSC Advances Accepted Manuscript

peak which located at 530.1 eV ($O_{lattice}$) attributed to O^{2-} ions on the wurtzite structure of a hexagonal Zn^{2+} ion array, which is surrounded by zinc atoms with the feeding of nearest-neighbor filled O^{2-} ions[44]. In addition, the oxygen species of Al-OH, Si-O-Si bonding groups which consist in HNTs may be covered by the O^{2-} surface deficient areas of ZnO [45]. The Zn-2p XPS spectrum (**Fig. 5**e) shows two symmetric peaks, the peak centered at 1044.6 eV is assigned to Zn $2p_{1/2}$ and another centered at 1021.1 eV is assigned to Zn $2p_{3/2}$, which indicating a normal status of Zn^{2+} in the g-C_3N_4-ZnO/HNTs nanocomposite [46].

Fig. 5. (a) XPS survey spectrum; high resolution scanning XPS of (b) C1s, (c) N1s; (d) O1s and (e) Zn-2p of g-C_3N_4-ZnO/HNTs nanocomposite.

3.5. UV-vis DRS

In order to investigate the optical properties and band structure of as-prepared composite photocatalysts, the HNTs, ZnO/HNTs and g-C_3N_4-ZnO/HNTs were carried out by UV-vis diffuse reflectance spectra (DRS) in **Fig. 6**. From the **Fig. 6**, the as-prepared ZnO/HNTs and g-C_3N_4-ZnO/HNTs photocatalysts have photoresponsed from UV light region to visible light region whereas the pure HNTs possess hardly any photoresponding abilities. As shown in **Fig. 6**, compared with the ZnO/HNTs, the absorption threshold values of the g-C_3N_4-ZnO/HNTs are extended up to the visible light region, which the main absorption edge exhibits red shift from 395 nm to 450 nm. The band gap energies of indirect transition semiconductor can

RSC Advances Accepted Manuscript

be calculated by the following Eq [47]:

$$(\alpha h\nu)^2 = A(h\nu - E_g) \quad (1)$$

Where α represents the absorption coefficient, h is Planck's constant, ν is the light frequency, A is a constant and E_g is the band gap energy. The band gap energy (E_g) of the resulting composite samples can be estimated from the intercept of tangents to the plots of $(\alpha h\nu)^2$ versus the photon energy ($h\nu$) are 3.12, 2.58 eV for ZnO/HNTs and g-C_3N_4-ZnO/HNTs respectively. The photon energy ($h\nu$) of g-C_3N_4-ZnO/HNTs is shown in the interior of **Fig. 6**. The band gap of g-C_3N_4-ZnO/HNTs (2.58 eV) is obviously narrower than ZnO/HNTs (3.12 eV), which can be attributed to the induction of g-C_3N_4 whose band gap is in the range of 2.4 ~ 2.7 eV reported in literatures[23, 48]. What's more, the band gap energy of ZnO/HNTs (3.13 eV) is slightly smaller than pure ZnO (3.2 eV), that can be attributed to the induction of HNTs which may be due to the surface synergistic interaction between HNTs and semiconductors [3, 33]. The results indicating that the as-prepared g-C_3N_4-ZnO/HNTs composite photocatalyst exhibited a better visible-light response ability than pure ZnO and ZnO/HNTs.

Fig. 6. UV-vis diffuse reflectance spectra of HNTs, ZnO/HNTs and g-C_3N_4-ZnO/HNTs composite photocatalysts.

3.6. BET analysis

It has been widely acknowledged that the morphology and crystal structure have a

RSC Advances Accepted Manuscript

significant impact on enhancing the photocatalytic ability of photocatalysts. **Table 1** exhibits the relationships between morphology and specific surface area. It is noted that the pore volume and average pore diameter increased with the increasing complexity of as-prepared composite photocatalysts. The pore volume and average pore diameter of pure halloysite nanotubes (HNTs) are 0.256 cm^3/g and 8.5 nm respectively which is the minimal comparing with the ZnO/HNTs and g-C_3N_4-ZnO/HNTs, and the g-C_3N_4-ZnO/HNTs composite photocatalysts possess a maximum pore structure, which can be observed in SEM (**Fig. 3**) and TEM (**Fig. 4**). In contrast, the BET surface areas of various samples are shown something special. It is worth noting that the S_{BET} value of ZnO/HNTs is 45.25 m^2/g which is smaller than the pure halloysite nanotubes (HNTs), whereas the g-C_3N_4-ZnO/HNTs displays a highest S_{BET} value of 50.06 m^2/g. This phenomenon may be attribute to the porthole effect of halloysite nanotubes (HNTs). Because of the two-layer aluminosilicate clay mineral material, which with the Si-O-Si on the external surface and Al-OH groups in the internal surface. When the ZnO nanoparticles composite with the HNTs, some of active nanoparticles block the pore and occupied a part of surface areas of the HNTs. After introducing the layered-shape g-C_3N_4, the g-C_3N_4-ZnO/HNTs reveals a larger S_{BET} value than ZnO/HNTs which is also larger than pure HNTs. The increase of BET surface area owed to the multi-storey or network structure of g-C_3N_4 that result in a large BET surface value. **Fig. S2** exhibits the nitrogen adsorption-desorption isotherms and Barrett-Joyner-Halenda (BJH) pore-size distribution curves of pure HNTs, ZnO/HNTs, and g-C_3N_4-ZnO/HNTs [19]. As shown in **Fig. S2**, the

RSC Advances Accepted Manuscript

adsorption-desorption isotherms of all samples are corresponding to typical type IV (BDDT Classification) with H1 hysteresis which indicate the meso-porous structures (2-50 nm) of all samples [49]. All of these results indicate that the ZnO nanoparticles are well loaded with HNTs and the composite g-C_3N_4 managed to increase the S_{BET} value which greatly enhanced the activities of as-prepared photocatalysts.

Table 1. Morphology and BET Surface Area of pure HNTs, ZnO/HNTs and g-C_3N_4-ZnO /HNTs Samples.

Sample	morphology	pore volume (cm^3/g)	pore diameter (nm)	BET surface area (m^2/g)
HNTs	nanotubes	0.256	8.5	47.45
ZnO/HNTs	tubes + particles	0.274	12.8	45.25
g-C_3N_4-ZnO/HNTs	tubes + particles + sheets	0.312	14.6	50.06

3.7. PL spectra

In order to investigate the fate of electron-hole pairs in semiconductors and reveal the efficiency of charge transfer, photon-generated carrier trapping, and separation of electron-hole pairs, the photoluminescence (PL) spectroscopy measurements, which result from the recombination of photo-excited electrons and holes, were carried out for g-C_3N_4 and g-C_3N_4-ZnO/HNTs. It is well acknowledged that the lower fluorescence intensity means higher separation efficiency of electron-hole pairs, which indicates the higher photocatalytic properties of the nanomaterials. **Fig. S3** displays PL spectra of the pure g-C_3N_4 (a), and g-C_3N_4-ZnO/HNTs composite (b). It can be clearly observed that the main emission peak for pure g-C_3N_4 appears at about 460 nm, which is equivalent to the band gap energy of pure g-C_3N_4 (2.7 eV), the

RSC Advances Accepted Manuscript

similar result is reported in other literatures [21]. After the ZnO/HNTs is introduced, the fluorescence intensity of g-C_3N_4-ZnO/HNTs decrease by a big margin compared to the pure g-C_3N_4, which indicates that the recombination rate of photo-generated charge carriers in g-C_3N_4-ZnO/HNTs heterojunction is much lower than pure g-C_3N_4. The mentions above confirm that there definitely exists the charge transfer between g-C_3N_4 and ZnO loading on HNTs. In addition, the tubular structure of HNTs could play important roles which as the appropriate supporters to improve the dispersity and surface area of the network or layered structure of g-C_3N_4, and thus to enhance the charge migration at the nano-interface. All these results exhibit an excellent performance of g-C_3N_4-ZnO/HNTs.

3.8. Photocatalytic activity

3.8.1. Photocatalytic activity study

The photocatalytic activity of as-prepared photocatalysts with different influencing factors were evaluated by photodegrading TC under visible light irradiation. The changes of TC concentration at different time intervals was investigated by measuring the absorption in UV-vis spectra at 357 nm. All the photocatalysts have 30 min in dark for getting the adsorption and desorption before irradiating by visible light. And the degradation ratio is calculated by the following equation [50]:

$$\eta = (\frac{C_0 - C_t}{C_0}) \times 100\% \quad (2)$$

Error! Reference source not found. Fig. S4 shows the influence on phorocatalytic activity of ZnO/HNTs with various calcination temperatures during the process of

RSC Advances Accepted Manuscript

synthetizing ZnO nanoparticles via calcining $Zn(NO_3)_2 \cdot 6H_2O$. It is obvious that 400 °C is the optimum temperature for preparation of the ZnO/HNTs compound photocatalyst which showed a highest photocatalytic activity via photodegrading TC solution approximately 50%. The samples fabricated at 300 and 800°C display much lower photocatalytic activity than other temperature condition, indicating that the reaction temperature plays an important role in the processes of the formation of ZnO/HNTs.

Fig. S5 displays the photocatalytic activity of ZnO/HNTs with the different contents of $Zn(NO_3)_2 \cdot 6H_2O$ which calcined at 400 ℃. As the primary activity component of ZnO/HNTs composite photocatalyst, the content of zinc oxide is significantly impacting the photocatalytic activity of composite photocatalyst. The blank control experiment was carried on which contained TC solution (20mg/L) only present 2.85% photocatalytic degradation for the photolysis of antibiotics [51]. Besides, the HNTs also present a little degradation which is attributed to absorption after the adsorption equilibrium status in 30 min[52, 53]. It can be seen from the **Fig. S5** that the photocatalytic activity is enhanced with the concentration of $Zn(NO_3)_2$ at 4.80 g/L and with a degradation rate of 0.030 min^{-1}. However, the activity of photocatalyst is not show a positive correlation with the ZnO content increasing from 4.80 g/L to 12.80 g/L as shown in **Fig. S5.** This is mainly due to the larger amount of e^- and h^+ when the content of ZnO increase, which result in a higher recombination rate of electron-hole pairs. Moreover, it is well known that the photocatalytic activity is depending on the dispersion degree of active constituent which is related to the monolayer dispersion

RSC Advances Accepted Manuscript

threshold. There is a most appropriate loading amount of ZnO on HNTs which can appear the maximum , that is a dispersion threshold where ZnO species are considered to cover the surface of HNTs in a monolayer state [54]. In addition, the accumulation and reunion of active nanoparticles could also be occurred if the loading amount of ZnO is superfluous, which will decrease the photocatalytic activity to a certain extent.

Fig. 7 illustrates the photo-degradation rate of g-C_3N_4-ZnO/HNTs with different content of g-C_3N_4 via degrading tetracycline. From the **Fig. 7**, the degradation of TC with various g-C_3N_4 content can be seen clearly and the pure g-C_3N_4 is measured for comparison. The photocatalytic rate is in the follow order: ZnO/HNTs < 100 wt% < pure g-C_3N_4 < 5 wt% < 50 wt% < 10 wt% < 20 wt%. The highest photocatalytic activity of 20 wt% g-C_3N_4 reach a photo-degradation rate at about 87% in 1 h under visible-light irradiation which is evidently higher than ZnO/HNTs with the concentration of $Zn(NO_3)_2$ at 4.80 g/L in **Fig. S5**. These indicating that the introduction of g-C_3N_4 which composited with ZnO/HNTs can actually enhance the visible light response ability and photocatalytic activity.

Fig. 7. Photocatalytic degradation of TC with g-C_3N_4-ZnO/HNTs (with different g-C_3N_4 contents) as photocatalysts under visible light irradiation.

3.8.2. Stability

Stability is a very important evidence to judge the quality of photocatalyst and for the further environmental application. The stabilities of the two ZnO/HNTs and g-C_3N_4-ZnO/HNTs composite photocatalysts were compared by multicycle repeated experiments for TC degradation under visible-light irradiation. The test results are

RSC Advances Accepted Manuscript

shown in **Fig. 8** and **Fig. 9**. There is a remarkable decrease of ZnO/HNTs compared with the initial value which blamed the photocorrosion and the self-decomposition of ZnO nanoparticles caused by the recombination of photo-generated electrons and holes[36]. The most worthwhile point in our work is that the stability of the final as-obtained samples enhanced obviously, only a slight decrease of photoactivity is observed after introducing the g-C_3N_4. The XRD analysis also verified the same result. **Fig. 9** presents the results of the XRD analysis before and after consecutive experiments and the key ZnO and g-C_3N_4 peaks are observed via comparing with the initial figure (**Fig. 2**b). The intensity of the figure only slightly lower than that before degradation. All of above results demonstrate convincingly that g-C_3N_4 could suppress the self-decomposition and photocorrosion of ZnO via compounding with ZnO/HNTs, which enhanced stability of g-C_3N_4-ZnO/HNTs efficiently.

Fig. 8. Cycling runs for the photocatalytic degradation of tetracycline by the prepared g-C_3N_4-ZnO/HNTs composite with 20 wt% g-C_3N_4 addition under visible-light irradiation.

Fig. 9. XRD patterns of g-C_3N_4-ZnO/HNTs before and after tetracycline degradation for the fourth cycle.

3.9. Photoelectrochemical experiments

3.9.1. Transient photocurrent response

The Incident-photon-to-current conversion efficiencies (IPCE) were measured for pure g-C_3N_4, pure ZnO, ZnO/HNTs and g-C_3N_4-ZnO/HNTs to analyze the

RSC Advances Accepted Manuscript

electronic interaction among g-C_3N_4, ZnO and HNTs, and confirm the prolonged lifetime of photo-generated charge carriers under visible-light irradiation with a pulse of 50 s, as shown in **Fig. 10**. It can be seen that distinct transient photocurrent responses were observed in the electrodes via on-off cycles, which may directly correlate with the recombination efficiency of photo-generated carriers[19]. Both ZnO/HNTs and g-C_3N_4-ZnO/HNTs composite photocatalysts exhibit higher photocurrents than pure g-C_3N_4 and ZnO, and the photocurrent of g-C_3N_4-ZnO/HNTs is the highest among all samples, indicating that g-C_3N_4-ZnO heterojunction of g-C_3N_4-ZnO/HNTs has an enhanced separation of photoinduced electron-hole pairs and can facilitate its photocatalytic activity greatly[24]. Moreover, a good photocurrent of ZnO/HNTs is displayed which may be contributed to the excellent physicochemical properties of halloysite nanotubes (HNTs) which enhanced the dispersity of photocatalysts, reduced the surface deficiency due to agglomeration and promoted rapid transfer of charge. In addition, the transfer resistance of electrons reduced with the decrease of the average size of ZnO nanoparticles, which contribute to the acceleration of electron transfer rate and enhancement of the intensity of photocurrent, respectively. A high electron transfer rate between semiconductor and surface (internal and outside) of HNTs [41]. The photoelectrochemical measurements of IPCE were described in supplementary information.

RSC Advances Accepted Manuscript

Fig. 10. Transient photocurrent response of g-C_3N_4 (a), pure ZnO (b), ZnO/HNTs (c) and g-C_3N_4-ZnO/HNTs nanocomposites (d) under visible-light irradiation (Init E = 0.5V, [Na_2SO_4] = 0.5 M).

3.9.2. Electrochemical impedance spectroscopy

As known to all that EIS is a powerful method for detecting the charge immigration across the semiconductor/electrolyte interface. In order to reveal the possible photocatalytic mechanism, the charge separation efficiency and the transfer resistance between photogenerated electrons and holes are examined by the electrochemical impedance spectra. **Fig. 11** shows the Nyquist plots of HNTs, pure g-C_3N_4, ZnO-HNTs and g-C_3N_4- ZnO/HNTs electrodes before and after visible light irradiation (λ > 420 nm). Generally, the arc radius in the EIS spectra reflects the interface layer impedance and the reaction rate occurring on the surface of the electrode[41, 55]. The arc radius of the EIS Nyquist plot of g-C_3N_4-ZnO/HNTs is smaller than ZnO/HNTs and pure g-C_3N_4, which implies a higher efficiency of charge transfer, more effective separation of photogererated electron-hole pairs. Furthermore, the arc radius of EIS Nyquist plot of g-C_3N_4-ZnO/HNTs under the visible light irradiation is smaller than that in dark, indicating the dramatically enhanced transfer and separation efficiency of photogenerated exciton and transfer rate of photoexcited electron after visible light irradiation[41, 43]. All of above results suggesting that the as-prepared g-C_3N_4-ZnO/HNTs composite structure can effectively inhibit the electron-hole recombination and contributed to the enhancement of photocatalytic activity, which is in good accordance with the result

RSC Advances Accepted Manuscript

of the transient photocurrent measurement.

Fig. 11. EIS plots for pure g-C_3N_4, pure HNTs, ZnO/HNTs and g-C_3N_4-ZnO/HNTs in the dark and g-C_3N_4-ZnO/HNTs under visible light illumination (Init E = 0.5V, [Na_2SO_4] = 0.5 M).

3.10. The mechanism of photodegradation

3.10.1. Active species trapping and quantification experiments

It has been widely recognized that active species have important impact on the photodegradation processes. To investigate the mechanism for the photodegradation of TC over g-C_3N_4-ZnO/HNTs, superoxide radical ($\bullet O_2^-$), hole (h^+), electron (e^-) and hydroxyl radical (•OH) were explored by employing different scavengers: benzoquinone (BQ), triethanolamine (TEOA), Ethanol and isopropyl alcohol (IPA) during the photocatalytic reaction, respectively. The experiment was started by 1 mmol quencher and the results are shown in **Fig. 12** [56]. The photocatalytic degradation rate of TC is 86.2% without scavengers. With the introduction of TEOA, BQ and IPA, the photocatalytic rates decreased to 13.4%, 23.3% and 28.7%, respectively. However, the degradation rate of TC was 82.9% after adding Ethanol while indicated that the e^- can be negligible in the reaction [57]. We can see clearly from the results that the h^+, $\bullet O_2^-$ and •OH are the main reactive species during the photocatalytic reaction system for g-C_3N_4-ZnO/HNTs photocatalyst. Moreover, the •OH plays the most important role which can be clearly observed in the schematic diagram (**Fig. 14**).

RSC Advances Accepted Manuscript

Fig. 12. The photocatalytic efficiency of g-C_3N_4-ZnO/HNTs with different quenchers in the photodegradation of tetracycline.

3.10.2. Analysis of photocatalytic mechanism

To confirm the mechanism further, the ESR spin-trap technique with DMPO was performed to investigate the presence of •OH and •O_2^- radicals in g-C_3N_4-ZnO/HNTs photocatalytic reaction systems under visible light illumination. DMPO can be used as an ideal radical scavenger contributed to DMPO can produce an adduct with hyperfine splitting, which due to both the nitroxide and the *β*–hydrogen [43]. As shown in **Fig. 13**, there is no signal could be detected. After visible light irradiation, the four characteristic peaks of the DMPO-•OH adducts (with a 1:2:2:1 intensity ratio, red line, **Fig. 13**a) and six characteristic peaks of DMPO •O_2^- adducts (**Fig. 13**b) in both H_2O and methanol are obviously observed in the ESR spectrum of the g-C_3N_4-ZnO/HNTs reaction system, which are consistent with the similar characteristic peaks reported by other groups for both the DMPO-•OH and DMPO •O_2^- adducts[58], indicating that the visible light irradiation is essential and effective for the generation of •OH and •O_2^- radicals on the surface of g-C_3N_4-ZnO/HNTs heterostructured photocatalysts. Therefore, according to both the active species trapping and quantification experiments and the ESR analysis, we can conclude that the •OH and •O_2^- exactly play major roles in the processes of degradation for TC.

Fig. 13. DMPO spin-trapping ESR spectra of g-C_3N_4-ZnO/HNTs samples in the dark and under

RSC Advances Accepted Manuscript

visible light irradiation at ambient temperature. (a) For DMPO-•OH in aqueous dispersion, and (b) for DMPO-•O_2^- in methanol dispersion.

One can see from above investigations that the g-C_3N_4-ZnO/HNTs photocatalyst not only enhanced stability evidently, but also exhibits a slightly higher photocatalytic activity than ZnO/HNTs before coupled with g-C_3N_4. The efficient charge separation of nanocomposite always be a crucial factor for the photocatalytic performances. The conduction band (CB) and valence band (VB) potentials of ZnO and g-C_3N_4 were also investigated to explain the enhanced photocatalytic mechanism.

The band edge potential of semiconductor photocatalysts is usual theoretically calculated via the equation as follows [59]:

$$E_{VB} = X - E_e + 0.5E_g \quad (3)$$

$$E_{CB} = E_{VB} - E_g \quad (4)$$

where E_{VB} and E_{CB} are the top of the VB edge potential and the bottom of CB edge potential which related to the normal hydrogen electrode (NHE) [59], X represents the Mulliken electronegativity of the component atoms in the semiconductor [60, 61]. E_g means the band gap energy of the photocatalyst and E_e is the energy of free electrons on the hydrogen scale (4.5 eV). It is widely admitted that both the CB (−1.13 V) and VB (+1.57 V) of g-C_3N_4 were negative than the CB (−0.5V) and VB (+2.8 eV) of ZnO [10, 20, 62], respectively. The g-C_3N_4-ZnO/HNTs composite photocatalyst is determined to be ca. 2.58 eV from the onset of UV-vis diffuse reflectance spectrum (DRS) in **Fig. 6**, which is slightly narrower than both pure g-C_3N_4 and ZnO.

RSC Advances Accepted Manuscript

Obviously, there is a separation and transfer process of photoexcited electron-hole carried out in the g-C_3N_4-ZnO/HNTs heterojunction. Basis of the above results, a possible mechanism for enhanced photocatalytic activity over the as-obtained g-C_3N_4-ZnO/HNTs nanocomposite is shown schematically in **Fig. 14**. When the sample is irradiated by visible light, the electron can be excited simultaneously from the CB of g-C_3N_4 to ZnO because the CB edge potential of g-C_3N_4 (−1.13 eV vs. NHE) is more negative than the CB edge potential of ZnO (−0.5 eV vs. NHE), while living the holes in the VB of g-C_3N_4. Subsequently, the special surface contact among g-C_3N_4, ZnO and HNTs which in the g-C_3N_4-ZnO/HNTs result in a rapid transfer and separation of the accumulated electrons, and effectively increased the photocatalytic properties of photocatalyst. The smooth close contact between various semiconductors is needed to accelerate the charge transfer and the calcination method we have utilized can be used to produce some chemical bonds which favoring the contact between semiconductors [37]. As shown in **Fig. 14**, it has a potential difference between CB edge potential of ZnO (−0.5 eV vs. NHE) and the standard redox potential E (O_2/•O_2^-) (−0.33 eV vs. NHE) so that the •O_2^- can be produced by the reaction of O_2 and e^- in CB. A continuous flow of active surface •OH groups would be produced in succession. On the basis of these datum, the photo-generated electrons in CB of g-C_3N_4 and ZnO are easily be transferred, however, the VB potential of g-C_3N_4 (1.57 eV vs. NHE) is more negative than the position of E (•OH/OH^-) which equal to 2.27 eV vs. NHE, leading to the photo-generated holes in the VB of g-C_3N_4 are difficultly oxidized OH^- or H_2O to

RSC Advances Accepted Manuscript

•OH. Consequently, the •OH, $•O_2^-$ and h^+ can be thought the main active species to responsible for the decomposition of organic pollutant, which is in agreement with the result of trapping experiment and ESR measurement. The major reactions can be described in Eq. (5) ~ (13) [56, 57]:

$$ZnO\text{-}g\text{-}C_3N_4/HNTs + h\nu \rightarrow ZnO\text{-}g\text{-}C_3N_4/HNTs + h^+ + e^- \quad (5)$$

$$h^+ + H_2O \rightarrow •OH + H^+ \quad (6)$$

$$e^- + O_2 \rightarrow •O_2^- \quad (7)$$

$$•O_2^- + H^+ \rightarrow •HO_2 \quad (8)$$

$$2e^- + O_2 + 2H^+ \rightarrow H_2O_2 \quad (9)$$

$$e^- + H^+ + •HO_2 \rightarrow H_2O_2 \quad (10)$$

$$e^- + H_2O_2 \rightarrow •OH + OH^- \quad (11)$$

$$•O_2^- + H_2O_2 \rightarrow •OH + OH^- + O_2 \quad (12)$$

$$•OH + TC \rightarrow \text{degradation products} \quad (13)$$

Fig. 14. Schematic diagram of the separation and transfer of photo-generated charge in g-C_3N_4-ZnO/HNTs composite under visible light irradiation.

4. Conclusions

In this study, we have successfully synthetized a visible-light-responsive g-C_3N_4-ZnO/HNTs nanocomposite heterojunction photocatalyst via introducing polymeric g-C_3N_4 with as-prepared ZnO/HNTs nanomaterial. The visible light photocatalytic activities were significantly enhanced compared to pure ZnO and g-C_3N_4. Compare to the ZnO/HNTs, the as-obtained g-C_3N_4-ZnO/HNTs composite

RSC Advances Accepted Manuscript

photocatalyst could not only enhance the photoresponsive ability in visible light region but also greatly improve the stability of photocatalyst via photodegrading the tetracycline. The highest photoactivity of 20 wt% g-C_3N_4-ZnO/HNTs composite photocatalyst should be attributed to the heterostructure of g-C_3N_4-ZnO which is clearly displayed by high-resolution transmission electron microscopy and coupling with the halloysite nanotubes, which provided a platform of active sites for photo-generated electrons and efficaciously suppressed the recombination reaction of photogenerated e^-/h^+ pairs. The possible mechanism for composite photocatalyst reveals a rapid transfer speed among various interfaces of different semiconductors, the •OH, $•O_2^-$ and h^+ are the main reactive species during the photocatalytic reaction system. In summary, a novel, efficient and stable fabricated photocatalyst is developed by a facile calcination method which has enormous potentials in the removal of organic pollutants exist in environment.

Acknowledgments

We gratefully acknowledge the financial support of the National Natural Science Foundation of China (No. 21576125, 21407064), the Natural Science Foundation of Jiangsu Province (BK20131259, BK20130489, BK20140532), and the Research Foundation of Jiangsu University, China (No. 11JDG107).

RSC Advances Accepted Manuscript

References

1. J. Xue, S. Ma, Y. Zhou, Z. Zhang and M. He, *ACS Appl. Mater. Interface*, 2015, **7**, 9630-9637.
2. C. Liu, D. Yang, Y. Jiao, Y. Tian, Y. Wang and Z. Jiang, *ACS Appl. Mater. Interface*, 2013, **5**, 3824-3832.
3. R. Wang, G. Jiang, Y. Ding, Y. Wang, X. Sun, X. Wang and W. Chen, *ACS Appl. Mater. Interface*, 2011, **3**, 4154-4158.
4. Z. W, L. W, J. Q.Wang, Q. Y, Y. Y, Y. Xie, K. Zhang, L. Wang, H. Fu and D. Zhao, *J. Am. Chem. Soc.*, 2014, **136**, 9280-9283.
5. S. Anandan, N. Ohashi and M. Miyauchi, *Appl. Catal. B: Environ.*, 2010, **100**, 502-509.
6. C. Li, T. Ahmed, M. Ma, T. Edvinsson and J. Zhu, *Appl. Catal. B: Environ.*, 2013, **138-139**, 175-183.
7. M. A. Henderson, *J. Catal.*, 2014, **318**, 53-60.
8. N. Zhang, R. Ciriminna, M. Pagliaro and Y. J. Xu, *Chem. Soc. Rev.*, 2014, **43**, 5276-5287.
9. Q. Deng, X. Duan, D. H. Ng, H. Tang, Y. Yang, M. Kong, Z. Wu, W. Cai and G. Wang, *ACS Appl. Mater. Interface*, 2012, **4**, 6030-6037.
10. J. Mu, C. Shao, Z. Guo, Z. Zhang, M. Zhang, P. Zhang, B. Chen and Y. Liu, *ACS Appl. Mater. Interface*, 2011, **3**, 590-596.
11. H. U. Lee, S. Y. Park, S. C. Lee, J. H. Seo, B. Son, H. Kim, H. J. Yun, G. W. Lee, S. M. Lee, B. Nam, J. W. Lee, Y. S. Huh, C. Jeon, H. J. Kim and J. Lee, *Appl. Catal. B: Environ.*, 2014, **144**, 83-89.
12. L. Wu, J. Li, S. Zhang, L. Long, X. Li and C. Cen, *J. Phys. Chem. C*, 2013, **117**, 22591-22597.
13. Z. Chen, N. Zhang and Y.-J. Xu, *CrystEngComm*, 2013, **15**, 3022-3030.

RSC Advances Accepted Manuscript

14. K. R. Reddy, V. G. Gomes and M. Hassan, *Mater. Res. Expr.*, 2014, **1**, 1-15.

15. B. M. Rajbongshi and S. K. Samdarshi, *Appl. Catal. B: Environ.*, 2014, **144**, 435-441.

16. B. Thongrom, P. Amornpitoksuk, S. Suwanboon and J. Baltrusaitis, *Korean J. Chem. Eng.*, 2014, **31**, 587-592.

17. W. He, H. Wu, W. G. Wamer, H. K. Kim, J. Zheng, H. Jia, Z. Zheng and J. J. Yin, *ACS Appl. Mater. Interface*, 2014, **6**, 15527-15535.

18. C. Eley, T. Li, F. Liao, S. M. Fairclough, J. M. Smith, G. Smith and S. C. Tsang, *Angew. Chem. Int. Ed.*, 2014, **53**, 7838-7842.

19. F. Dong, Z. Zhao, T. Xiong, Z. Ni, W. Zhang, Y. Sun and W. K. Ho, *ACS Appl. Mater. Interface*, 2013, **5**, 11392-11401.

20. D. Wang, H. Sun, Q. Luo, X. Yang and R. Yin, *Appl. Catal. B: Environ.*, 2014, **156-157**, 323-330.

21. G. Dong, Y. Zhang, Q. Pan and J. Qiu, *J. Photoch. Photobio. C*, 2014, **20**, 33-50.

22. Y. Gong, P. Zhang, X. Xu, Y. Li, H. Li and Y. Wang, *J. Catal.*, 2013, **297**, 272-280.

23. X.-J. Wang, W.-Y. Yang, F.-T. Li, Y.-B. Xue, R.-H. Liu and Y.-J. Hao, *Ind. Eng. Chem. Res.*, 2013, **52**, 17140-17150.

24. K. Wang, Q. Li, B. Liu, B. Cheng, W. Ho and J. Yu, *Appl. Catal. B: Environ.*, 2015, **176**, 44-52.

25. K. Dai, L. H. Lu, C. H. Liang, Q. Liu and G. Zhu, *Appl. Catal. B: Environ.*, 2014, **156-157**, 331-340.

26. D. Xia, Z. Shen, G. Huang, W. Wang, J. C. Yu and P. K. Wong, *Environ. Sci. Technol.*, 2015, **49**, 6264-6273.

RSC Advances Accepted Manuscript

27. X. Bai, R. Zong, C. Li, D. Liu, Y. Liu and Y. Zhu, *Appl. Catal. B: Environ.*, 2014, **147**, 82-91.

28. X. Dai, M. Xie, S. Meng, X. Fu and S. Chen, *Appl. Catal. B: Environ.*, 2014, **158-159**, 382-390.

29. L. Ge, C. Han and J. Liu, *Appl. Catal. B: Environ.*, 2011, **108-109**, 100-107.

30. X. Guan and L. Guo, *ACS Catal.*, 2014, **4**, 3020-3026.

31. B. Mu, W. Zhang and A. Wang, *J. Mater. Sci*, 2014, **49**, 7181-7191.

32. W. Xing, L. Ni, P. Huo, Z. Lu, X. Liu, Y. Luo and Y. Yan, *Appl. Surf. Sci.*, 2012, **259**, 698-704.

33. G. Cavallaro, G. Lazzara, S. Milioto, F. Parisi and V. Sanzillo, *ACS Appl. Mater. Interface*, 2014, **6**, 606-612.

34. M. Makaremi, R. T. De Silva and P. Pasbakhsh, *J. Phys. Chem. C*, 2015, **119**, 7949-7958.

35. G. D. Wright, *ACS Infect. Dis.*, 2015, **1**, 80-84.

36. P. J. Frappaolo, *ACS SYM. SER.*, 1986, **320**, 100-111.

37. Y. He, J. Cai, L. Zhang, X. Wang, H. Lin, B. Teng, L. Zhao, W. Weng, H. Wan and M. Fan, *Ind. Eng. Chem. Res.*, 2014, **53**, 5905-5915.

38. G. Dong and L. Zhang, *J. Phys. Chem. C*, 2013, **117**, 4062-4068.

39. H. Wang, L. Zhang, Z. Chen, J. Hu, S. Li, Z. Wang, J. Liu and X. Wang, *Chem. Soc. Rev.*, 2014, **43**, 5234-5244.

40. Y. Zhang, Y. Xie, A. Tang, Y. Zhou, J. Ouyang and H. Yang, *Ind. Eng. Chem. Res.*, 2014, **53**, 5507-5514.

41. D. Chen, K. Wang, W. Hong, R. Zong, W. Yao and Y. Zhu, *Appl. Catal. B: Environ.*, 2015, **166-167**, 366-373.

42. F. Dong, L. Wu, Y. Sun, M. Fu, Z. Wu and S. C. Lee, *J. Mater. Chem.*, 2011, **21**, 15171-15174.

RSC Advances Accepted Manuscript

43. X. Bai, L. Wang, R. Zong and Y. Zhu, *J. Phys. Chem. C*, 2013, **117**, 9952-9961.

44. D. E. Motaung, G. H. Mhlongo, S. S. Nkosi, G. F. Malgas, B. W. Mwakikunga, E. Coetsee, H. C. Swart, H. M. Abdallah, T. Moyo and S. S. Ray, *ACS Appl. Mater. Interface*, 2014, **6**, 8981-8995.

45. J. B. Goodall, D. Illsley, R. Lines, N. M. Makwana and J. A. Darr, *ACS Comb. Sci.*, 2015, **17**, 100-112.

46. X. Zhang, C. Shao, Z. Zhang, J. Li, P. Zhang, M. Zhang, J. Mu, Z. Guo, P. Liang and Y. Liu, *ACS Appl. Mater. Interface*, 2012, **4**, 785-790.

47. M. Mazur, J. Domaradzki and D. Wojcieszak, *Bull. Pol. Ac.: Tech.*, 2014, **62**, 583-588.

48. Y. Tian, B. Chang, J. Lu, J. Fu, F. Xi and X. Dong, *ACS Appl. Mater. Interface*, 2013, **5**, 7079-7085.

49. T. C. Wang, W. Bury, D. A. Gomez-Gualdron, N. A. Vermeulen, J. E. Mondloch, P. Deria, K. Zhang, P. Z. Moghadam, A. A. Sarjeant, R. Q. Snurr, J. F. Stoddart, J. T. Hupp and O. K. Farha, *J. Am. Chem. Soc.*, 2015, **137**, 3585-3591.

50. M. Zhou, D. Han, X. Liu, C. Ma, H. Wang, Y. Tang, P. Huo, W. Shi, Y. Yan and J. Yang, *Appl. Catal. B: Environ.*, 2015, **172-173**, 174-184.

51. B. L. Edhlund, W.A. Arnold and K. Mcneill, *Environ. Sci. Technol.*, 2006, 40, 5422-5427.

52. Y. Zhang, A. Tang, H. Yang and J. Ouyang, *Appl. Clay Sci.*, 2015, 10.1016/j. 2015. 06. 034.

53. Y. Zhang, H. Yang, *Phys. Chem. Miner*., 2012, 39, 789-795.

54. K. Song, H. Zhang, Y. Zhang, Y. Tang and K. Tang, *J. Catal.*, 2013, **299**, 119-128.

55. S. A. Ansari, M. M. Khan, M. O. Ansari, J. Lee and M. H. Cho, *J. Phys. Chem. C*, 2013, **117**, 27023-27030.

RSC Advances Accepted Manuscript

56. H. Lv, G. Ji, Z. Yang, Y. Liu, X. Zhang, W. Liu and H. Zhang, *J. Colloid Interf. Sci*, 2015, **450**, 381-387.

57. W. Liu, M. Wang, C. Xu and S. Chen, *Chem. Eng. J.*, 2012, **209**, 386-393.

58. X. Li, S. Fang, L. Ge, C. Han, P. Qiu and W. Liu, *Appl. Catal. B: Environ.*, 2015, **176**, 62-69.

59. H. Shi, G. Chen, C. Zhang and Z. Zou, *ACS Catal.*, 2014, **4**, 3637-3643.

60. M. A. BUTLER and D. S. GINLEY, *J. Mater. Sci*, 1980, **15**, 1-19.

61. H. Shi, G. Chen and Z. Zou, *Appl. Catal. B: Environ.*, 2014, **156-157**, 378-384.

62. Y. Liu, Y. Hu, M. Zhou, H. Qian and X. Hu, *Appl. Catal. B: Environ.*, 2012, **125**, 425-431.

RSC Advances Accepted Manuscript

Figure captions

Fig. 1. The schematic illustration on formation of g-C_3N_4-ZnO/HNTs composite photocatalyst.

Fig. 2. XRD patterns of (a) pure ZnO, g-C_3N_4 and g-C_3N_4-ZnO/HNTs and (b) different content of g-C_3N_4 composite photocatalysts.

Fig. 3. SEM and EDS images of (a, b) HNTs, (c, d) ZnO/HNTs, (e, f) g-C_3N_4-ZnO/HNTs.

Fig. 4. (a) TEM image of pure HNTs. (b) TEM image of ZnO/HNTs. (c) TEM image of g-C_3N_4-ZnO/HNTs. (d) HRTEM image of g-C_3N_4-ZnO/HNTs photocatalysts

Fig. 5. (a) XPS survey spectrum; high resolution scanning XPS of (b) C1s, (c) N1s; (d) O1s and (e) Zn-2p of g-C_3N_4-ZnO/HNTs nanocomposite.

Fig. 6. UV-vis diffuse reflectance spectra of HNTs, ZnO/HNTs and g-C_3N_4-ZnO/HNTs composite photocatalysts.

Fig. 7. Photocatalytic degradation of TC with g-C_3N_4-ZnO/HNTs (with different g-C_3N_4 contents) as photocatalysts under visible light irradiation.

Fig. 8. Cycling runs for the photocatalytic degradation of tetracycline by the prepared g-C_3N_4-ZnO/HNTs composite with 20 wt% g-C_3N_4 addition under visible-light irradiation.

Fig. 9. XRD patterns of g-C_3N_4-ZnO/HNTs before and after tetracycline degradation for the fourth cycle**.**

Fig. 10. Transient photocurrent response of g-C_3N_4 (a), pure ZnO (b), ZnO/HNTs (c) and g-C_3N_4-ZnO/HNTs nanocomposites (d) under visible-light irradiation (Init E = 0.5V, [Na_2SO_4] = 0.5 M).

Fig. 11. EIS plots for pure g-C_3N_4, pure HNTs, ZnO/HNTs and g-C_3N_4-ZnO/HNTs in the dark and g-C_3N_4-ZnO/HNTs under visible light illumination (Init E = 0.5V, [Na_2SO_4] = 0.5 M).

RSC Advances Accepted Manuscript

Fig. 12. The photocatalytic efficiency of g-C_3N_4-ZnO/HNTs with different quenchers in the photodegradation of tetracycline.

Fig. 13. DMPO spin-trapping ESR spectra of g-C_3N_4-ZnO/HNTs samples in the dark and under VL irradiation at ambient temperature. (a) For DMPO-•OH in aqueous dispersion, and (b) for DMPO-•O_2^- in methanol dispersion.

Fig. 14. Schematic diagram of the separation and transfer of photo-generated charge in g-C_3N_4-ZnO/HNTs composite under visible light irradiation.

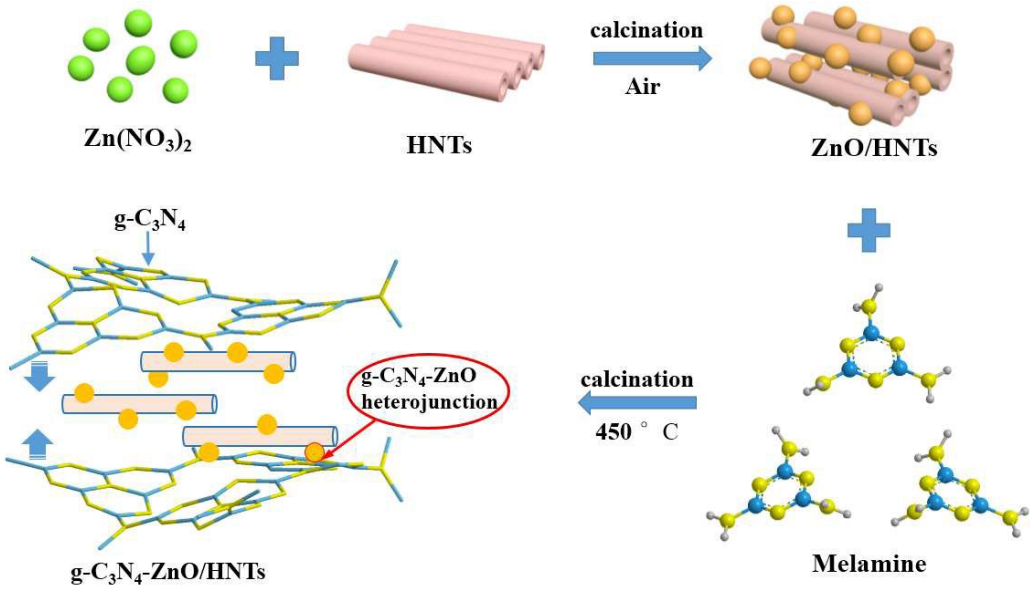

Fig. 1. The schematic illustration on formation of g-C_3N_4-ZnO/HNTs composite photocatalyst.

RSC Advances Accepted Manuscript

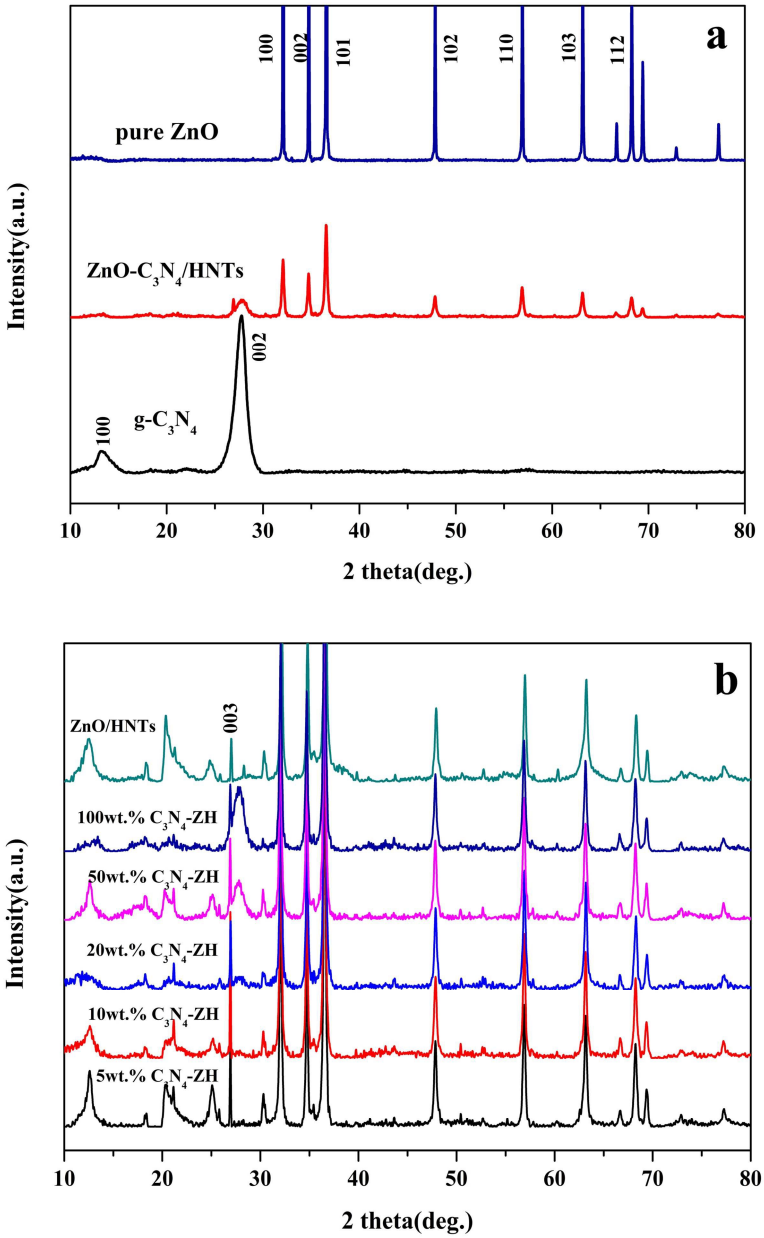

Fig. 2. XRD patterns of (a) pure ZnO, g-C_3N_4 and g-C_3N_4-ZnO/HNTs and (b) different content of g-C_3N_4 composite photocatalysts.

RSC Advances Accepted Manuscript

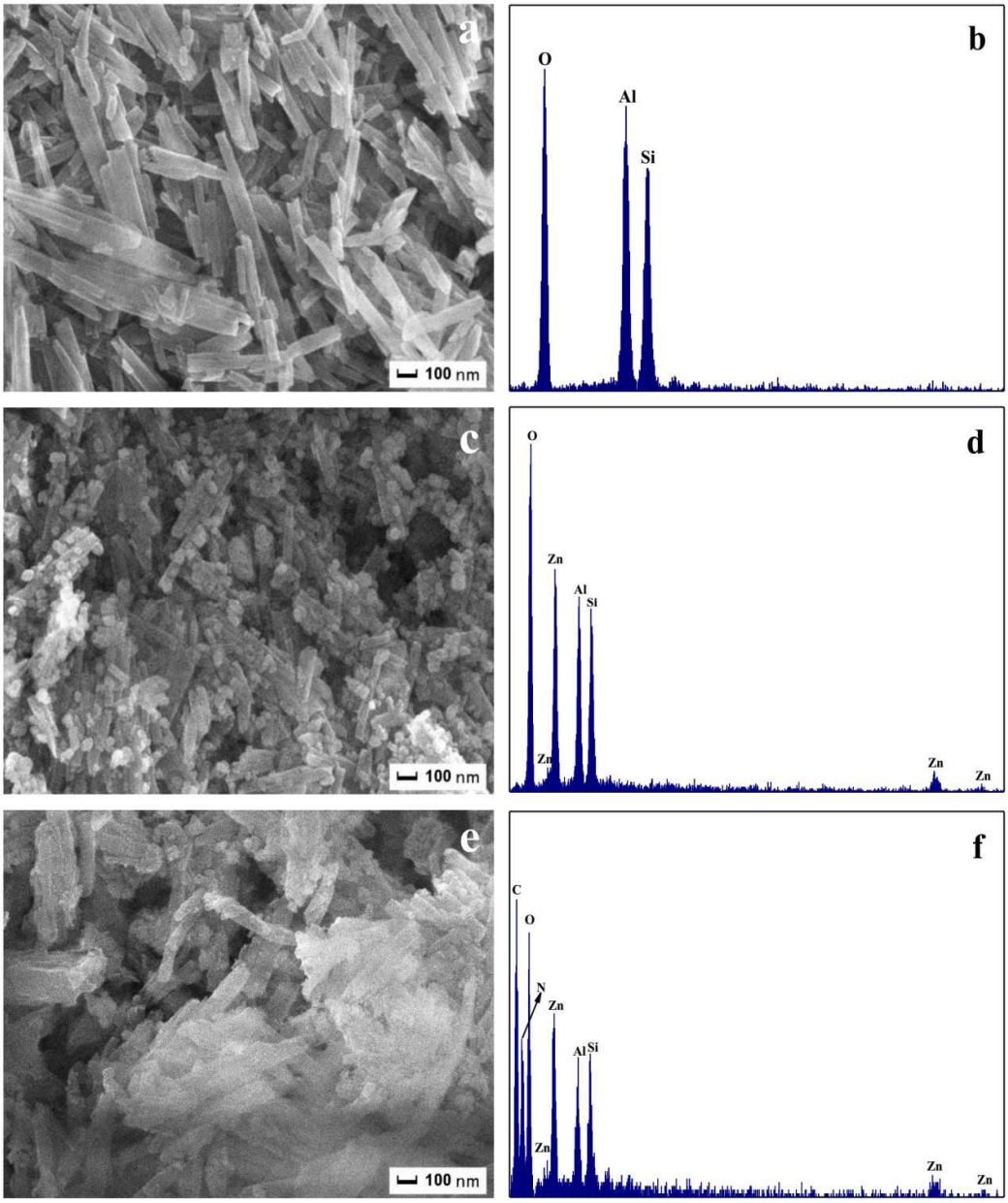

Fig. 3. SEM and EDS images of (a, b) HNTs, (c, d) ZnO/HNTs, (e, f) g-C_3N_4-ZnO/HNTs.

RSC Advances Accepted Manuscript

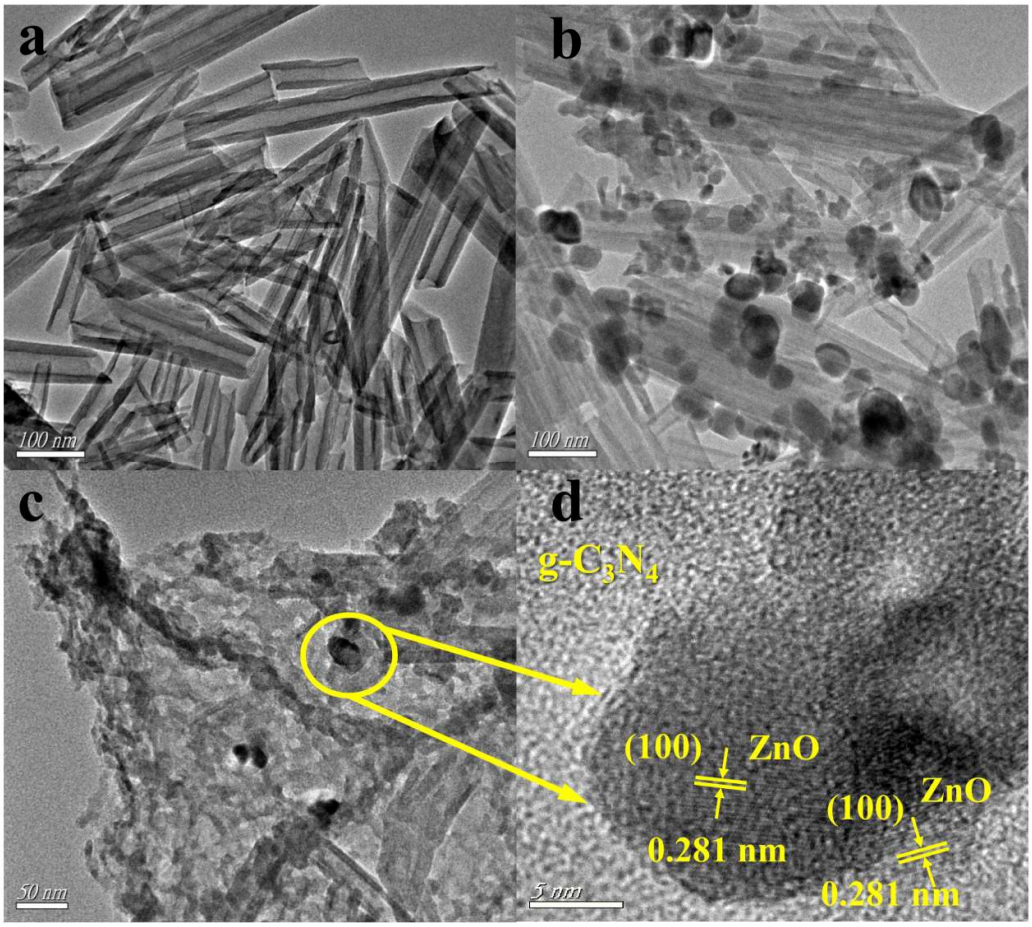

Fig. 4. (a) TEM image of pure HNTs. (b) TEM image of ZnO/HNTs. (c) TEM image of g-C_3N_4-ZnO/HNTs. (d) HRTEM image of g-C_3N_4-ZnO/HNTs photocatalysts.

RSC Advances Accepted Manuscript

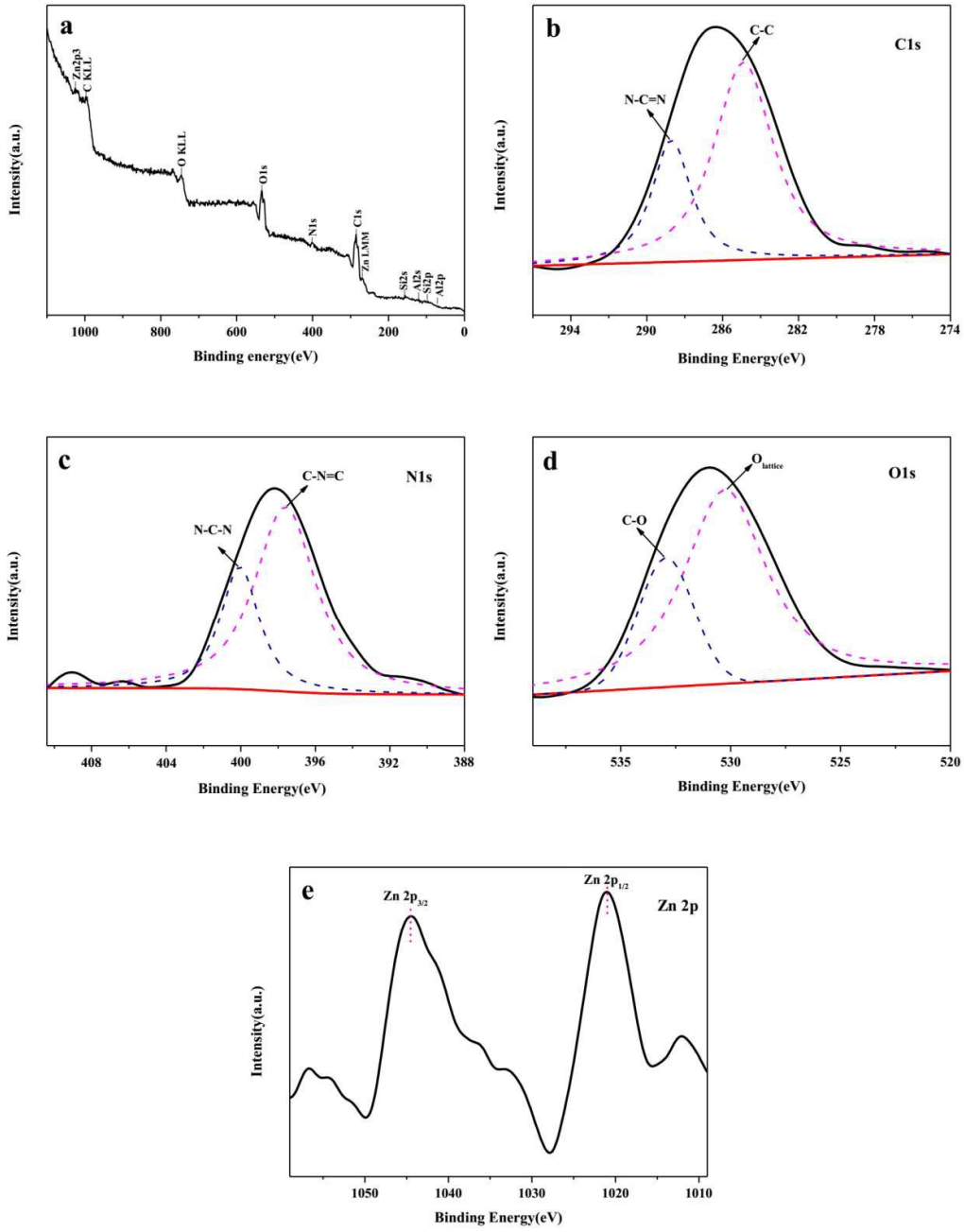

Fig. 5. (a) XPS survey spectrum; high resolution scanning XPS of (b) C1s, (c) N1s; (d) O1s and (e) Zn-2p of g-C_3N_4-ZnO/HNTs nanocomposite.

RSC Advances Accepted Manuscript

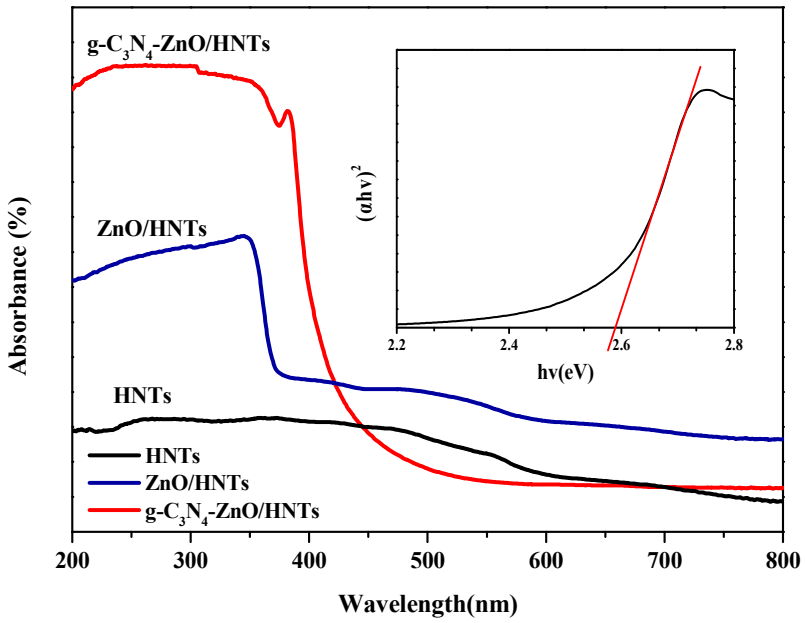

Fig. 6. UV-vis diffuse reflectance spectra of HNTs, ZnO/HNTs and g-C_3N_4-ZnO/HNTs composite photocatalysts.

RSC Advances Accepted Manuscript

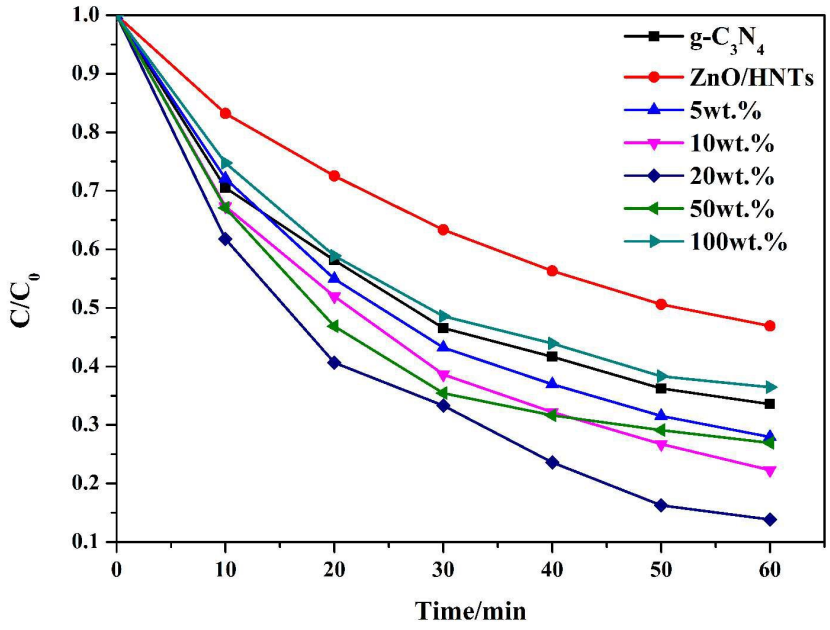

Fig. 7. Photocatalytic degradation of TC with g-C_3N_4-ZnO/HNTs (with different g-C_3N_4 contents) as photocatalysts under visible light irradiation.

RSC Advances Accepted Manuscript

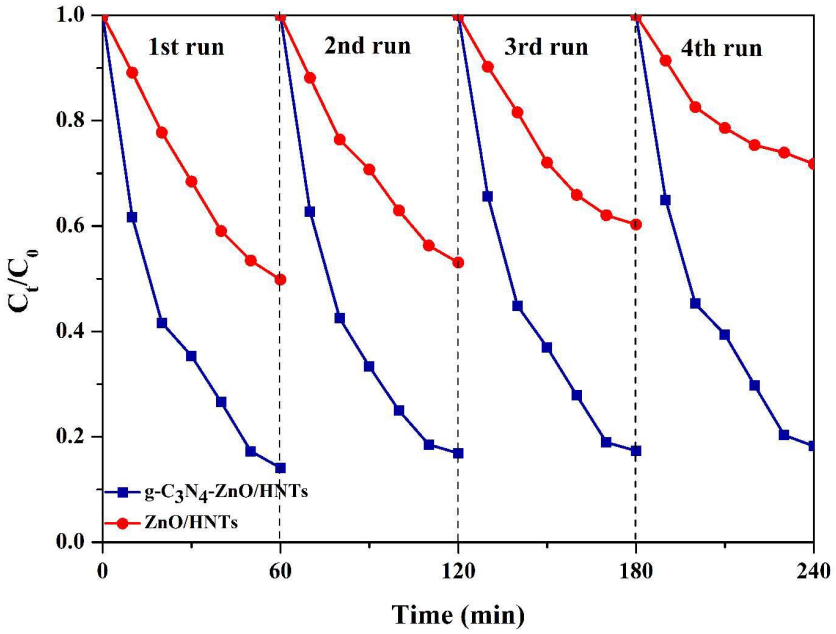

Fig. 8. Cycling runs for the photocatalytic degradation of tetracycline by the prepared g-C_3N_4-ZnO/HNTs composite with 20 wt% g-C_3N_4 addition under visible-light irradiation.

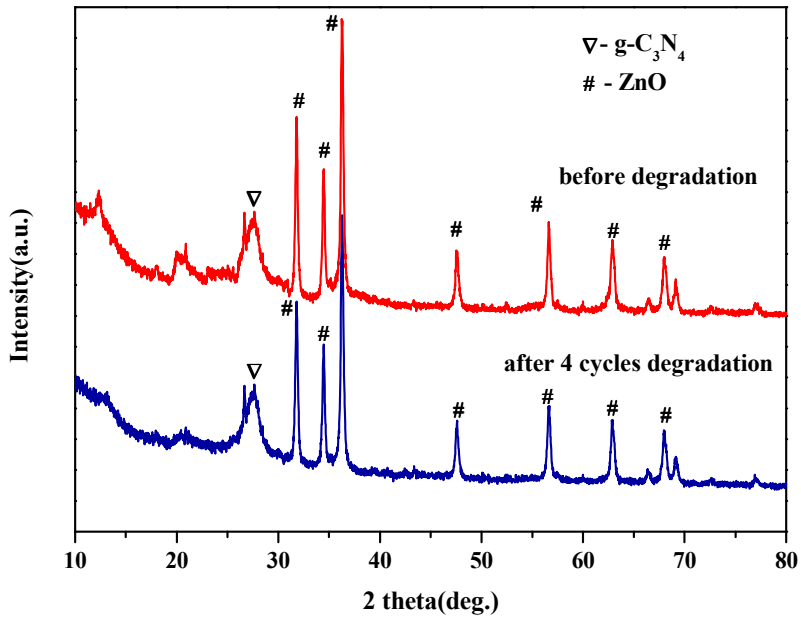

Fig. 9. XRD patterns of g-C_3N_4-ZnO/HNTs before and after tetracycline degradation for the fourth cycle.

RSC Advances Accepted Manuscript

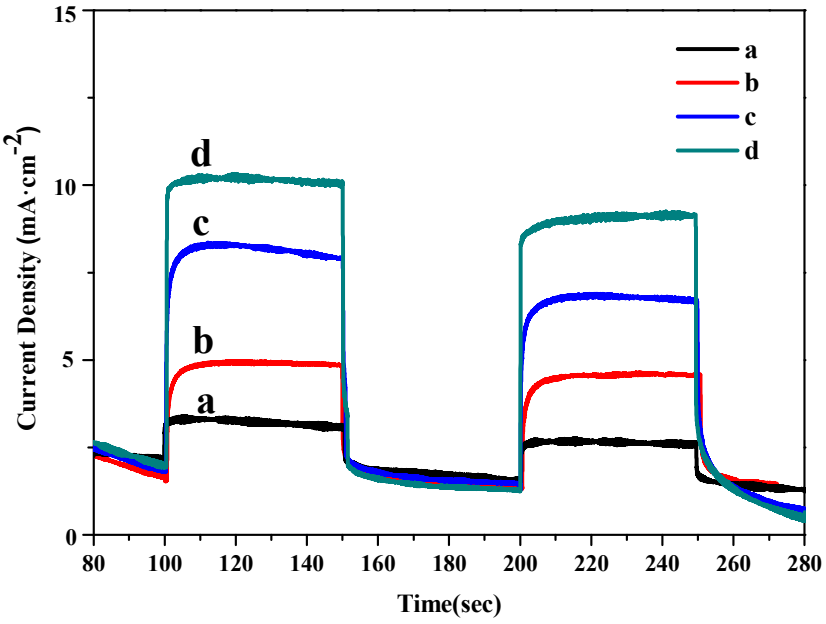

Fig. 10. Transient photocurrent response of g-C_3N_4 (a), pure ZnO (b), ZnO/HNTs (c) and g-C_3N_4-ZnO/HNTs nanocomposites (d) under visible-light irradiation (Init E = 0.5V, [Na_2SO_4] = 0.5 M).

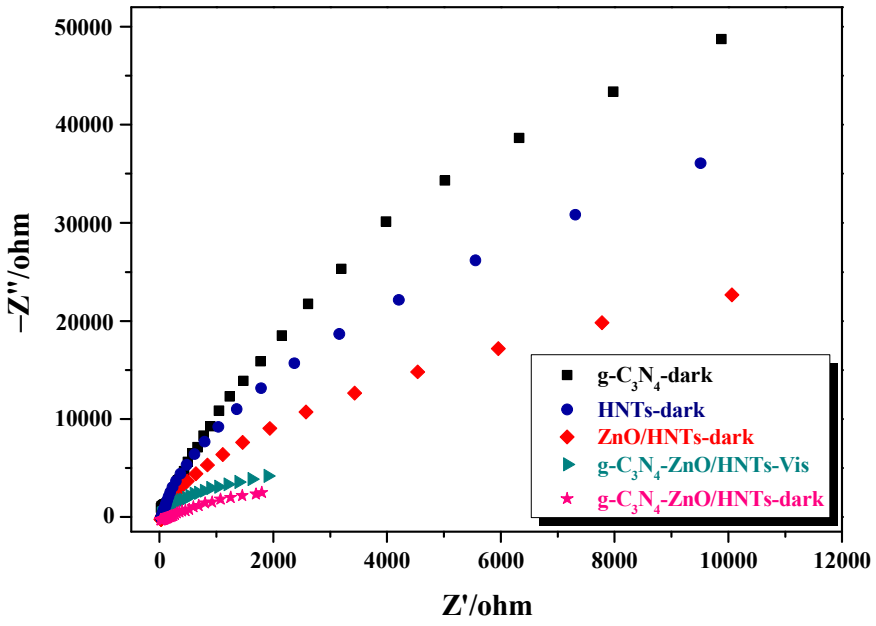

Fig. 11. EIS plots for pure g-C_3N_4, pure HNTs, ZnO/HNTs and g-C_3N_4-ZnO/HNTs in the dark and g-C_3N_4-ZnO/HNTs under visible light illumination (Init E = 0.5V, [Na_2SO_4] = 0.5 M).

RSC Advances Accepted Manuscript

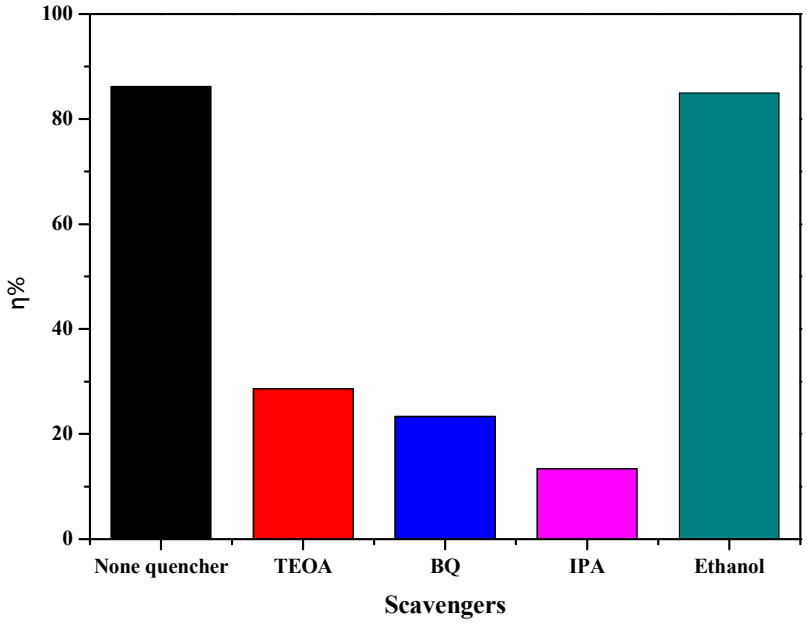

Fig. 12. The photocatalytic efficiency of g-C_3N_4-ZnO/HNTs with different quenchers in the photodegradation of tetracycline.

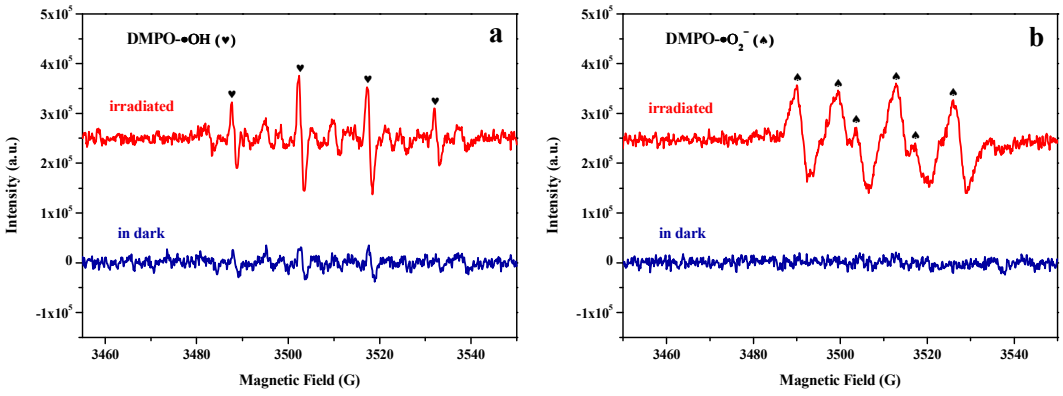

Fig. 13. DMPO spin-trapping ESR spectra of g-C_3N_4-ZnO/HNTs samples in the dark and under VL irradiation at ambient temperature. (a) For DMPO-•OH in aqueous dispersion, and (b) for DMPO-•O_2^- in methanol dispersion.

RSC Advances Accepted Manuscript

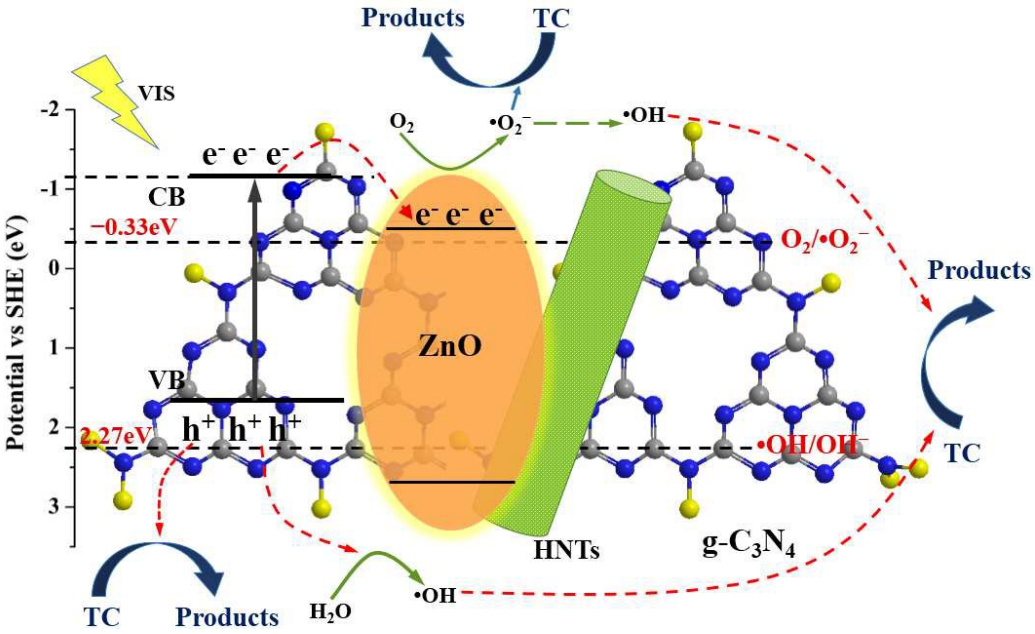

Fig. 14. Schematic diagram of the separation and transfer of photo-generated charge in g-C_3N_4-ZnO/HNTs composite under visible light irradiation.

RSC Advances Accepted Manuscript